Lawrence Berkeley National Laboratory

Title

Origin of Rapid Delithiation In Secondary Particles Of LiNi0.8Co0.15Al0.05O2 and LiNiyMnzCo1−y−zO2 Cathodes

Permalink

https://escholarship.org/uc/item/0t77k1nw

Journal

Advanced Energy Materials, 13(37)

ISSN

1614-6832

Authors

Wolfman, Mark
May, Brian M
Goel, Vishwas
et al.

Publication Date

2023-10-01

DOI

10.1002/aenm.202300895

Copyright Information

Peer reviewed

Origin of Rapid Delithiation In Secondary Particles Of LiNi$_{0.8}$Co$_{0.15}$Al$_{0.05}$O$_2$ and LiNi$_y$Mn$_z$Co$_{1-y-z}$O$_2$ Cathodes

Mark Wolfman, Brian M. May, Vishwas Goel, Sicen Du, Young-Sang Yu, Nicholas V. Faenza, Nathalie Pereira, Antonin Grenier, Kamila M. Wiaderek, Ruqing Xu, Jiajun Wang, Karena W. Chapman, Glenn G. Amatucci, Katsuyo Thornton, and Jordi Cabana*

Most research on the electrochemical dynamics in materials for high-energy Li-ion batteries has focused on the global behavior of the electrode. This approach is susceptible to misleading analyses resulting from idiosyncratic kinetic conditions, such as surface impurities inducing an apparent two-phase transformation within LiNi$_{0.8}$Co$_{0.15}$Al$_{0.05}$O$_2$. Here, nano-focused X-ray probes are used to measure delithiation operando at the scale of secondary particle agglomerates in layered cathode materials during charge. After an initial latent phase, individual secondary particles undergo rapid, stochastic, and largely uniform delithiation, which is in contrast with the gradual increase in cell potential. This behavior reproduces across several layered oxides. Operando X-ray microdiffraction (µ-XRD) leverages the relationship between Li content and lattice parameter to further reveal that rate acceleration occurs between Li-site fraction (x_{Li}) ≈0.9 and ≈0.5 for LiNi$_{0.8}$Co$_{0.15}$Al$_{0.05}$O$_2$. Physics-based modeling shows that, to reproduce the experimental results, the exchange current density (i_0) must depend on x_{Li}, and that i_0 should increase rapidly over three orders of magnitude at the transition point. The specifics and implications of this jump in i_0 are crucial to understanding the charge-storage reaction of Li-ion battery cathodes.

1. Introduction

Layered transition metal oxides represent the state-of-the-art cathode materials for electrochemical energy storage in Li-ion batteries. In order to meet ever more ambitious performance targets, it is necessary to improve their efficiency and reliability beyond existing limitations. While layered cathodes provide high theoretical capacity, maintaining cycling stability requires lower charge cut-off potentials wherein only ≈70 % of the theoretical capacity is realistically achievable, a challenge aggravated at higher rates of charge and discharge.[1,2] Fundamentally, these limitations are underpinned by the interplay between thermodynamic and kinetic relationships in the chemical transformations required for full utilization of the cathode. Thus, defining these intrinsic relationships remains foundational to the design of batteries that surpass

M. Wolfman, B. M. May, J. Cabana
Department of Chemistry
University of Illinois at Chicago
845 W Taylor St, 4500 SES (MC 111), Chicago, IL 60607, USA
E-mail: jcabana@uic.edu
M. Wolfman
Chemical Sciences and Engineering Division
Argonne National Laboratory
9700 S Cass Ave, Lemont, IL 60439, USA

M. Wolfman, K. M. Wiaderek, R. Xu
X-ray Science Division, Advanced Photon Source
Argonne National Laboratory
9700 S Cass Ave, Lemont, IL 60439, USA
V. Goel, S. Du, K. Thornton
Department of Materials Science and Engineering
University of Michigan
2300 Hayward St, Ann Arbor, MI 48109, USA
Y.-S. Yu
Advanced Light Source
Lawrence Berkeley National Laboratory
6 Cyclotron Rd, Berkeley, CA 94720, USA
Y.-S. Yu
Department of Physics
Chungbuk National University
Chungdae-ro 1, Seowon-Gu, Cheongju, Chungbuk 28644, South Korea
N. V. Faenza, N. Pereira, G. G. Amatucci
Energy Storage Research Group, Department of Materials Science and Engineering
Rutgers, The State University of New Jersey

**ADVANCED
SCIENCE NEWS**

www.advancedsciencenews.com

**ADVANCED
ENERGY
MATERIALS**

www.advenergymat.de

existing bottlenecks. Careful observation of the behavior of individual particles bypasses the confounding factors arising from local heterogeneity at the level of the electrode ensemble. These observations can then be combined with detailed simulation of the underlying electrochemical processes to reveal the factors governing these reactions, ultimately guiding the engineering of energy storage systems with superior performance.

Analytical techniques based on X-ray probes are indispensable to characterize chemical phenomena in solid materials like layered oxide cathodes.[3] Furthermore, synchrotron X-ray characterization provides several methodologies of imaging and mapping that are highly suited to evaluate local chemical events and heterogeneity,[4] at spatial resolutions sufficient to unfold observations among and within secondary particles typically found in commercial materials. Among them, μ-XRD extends the structural characterization capability of conventional powder X-ray diffraction (PXRD) with up to sub-micrometer resolution. In μ-XRD, incoming X-rays are focused to a sub-micron spot and scanned over individual secondary particles. At each mapping position, the diffraction pattern captured by an area detector provides details of the crystal structure, like the lattice parameters, which can then be related to chemical states (e.g., extent of lithiation). A complementary technique, transmission X-ray microscopy (TXM), produces projection micrographs showing the optical depth of the object with ≈30 nm spatial resolution, depending on the instrument configuration. The tunable nature of synchrotron X-ray sources allows micrographs of the same field of view to be captured at several energies. To produce chemical maps, images are collected at a range of energies spanning an X-ray absorption edge, which produce a separate spectrum for each pixel in the field of view and a map with chemical significance (e.g., metal oxidation states) after data reduction. For both techniques, since the individual measurements are projections through the specimen, the resulting maps show the average state through the optical axis (perpendicular to the image plane).

Beyond the specific spatial and chemical insight, the long penetration depth provided by hard X-rays (i.e., with energies above 4000 eV) available at synchrotrons provides degrees of transmissibility that make these techniques compatible with measurements inside an assembled, albeit modified, electrochemical cell (in situ) and, ideally, while it is actively cycling (operando). In addition to avoiding relaxation effects, operando measurements allow the same object to be measured repeatedly at different states of charge. Tracking the same object during a cycle allows for a direct comparison between different states of charge and provides a clearer picture of the evolution of spatial heterogeneity.

Operando PXRD, which averages the diffraction signal over the ensemble of the cathode, is the premier tool to probe the transformation of layered oxides undergoing electrochemical reactions because it reveals phase progressions that have

implications for solid-state kinetics and mechanical strain. In $LiNi_yMn_zCo_{1-y-z}O_2$ materials like $LiNi_{1/3}Mn_{1/3}Co_{1/3}O_2$, PXRD measurements have revealed that the transformation follows a mechanism involving a single phase in the range of voltages used in practical applications,[5–7] with the formation of material fractions within the same solid-solution regime but with different Li contents and, thus, degrees of oxidation of the transition metals. While $LiNi_{0.8}Co_{0.15}Al_{0.05}O_2$ was expected to follow a similar mechanism, the first report described the transformation following a mixture of two phases, rather than a single solid solution, during the first charge when stored in ambient conditions, followed by a single-phase (solid solution) transformation seen during subsequent charge cycles.[8] Kinetic manipulation of $LiNi_{1/3}Mn_{1/3}Co_{1/3}O_2$ can be used to induce the co-existence of two crystallographic phases with a small difference in a and c lattice parameters over a narrow composition range.[9,10] While impurities forming blocking surface layers help explain a seemingly two-phase transformation,[11] limitations arising from diffusion kinetics within the material have also been proposed.[12] Recently, this apparent two-phase behavior in layered oxides has been connected to individual particles delithiating rapidly and at seemingly random times,[13–16] but conflicting explanations for this behavior are presented. Park et al.[13] used in situ PXRD to indirectly study the transformation kinetics of $LiNi_{1/3}Mn_{1/3}Co_{1/3}O_2$ and showed that interfacial exchange current is the underlying reason for the observed pseudo-two-phase behavior rather than the solid-state diffusion limitation. In the same report, ex-situ X-ray microscopy revealed secondary particles in disparate states of charge from one another. In separate work with $LiNi_{0.5}Mn_{0.3}Co_{0.2}O_2$ particles,[14] direct observations of asynchronous delithiation were attributed to spatial inhomogeneity in the electrostatic potential caused by limitations in electrical conductivity due to the incomplete coverage of the particles by carbon additives. Lastly, Merryweather et al.[15] and Ge et al.[16] ascribed the sudden changes in rates of delithiation in different layered oxides to sluggish solid-state transport in the Li-rich phase. Clearly, there is no clear consensus on the origin of this rapid delithiation behavior in layered cathode particles. Therefore, the oxidation dynamics of these layered cathode materials warrant further study to clarify the behavior and asynchronicity of the individual secondary particles that typically compose a cathode in order to uncover sources of kinetic limitations that must be overcome by architecture design.

Here, we examined the mechanism of transformation in secondary particles of established layered cathode materials, namely $LiNi_{0.8}Co_{0.15}Al_{0.05}O_2$, $LiNi_{1/3}Mn_{1/3}Co_{1/3}O_2$, and $LiNi_{0.5}Mn_{0.3}Co_{0.2}O_2$. A combination of operando μ-XRD and TXM X-ray absorbance spectroscopy (XAS) experiments probed the evolution of the local state of charge in the secondary particles of these materials. Consistent with other reports, despite cycling at constant current, individual particles exhibited a sharp and stochastic transition from an initial, latent state to a high state of charge. The μ-XRD analysis of $LiNi_{0.8}Co_{0.15}Al_{0.05}O_2$ revealed individual particles following a solid-solution mechanism, and a domain of fast delithiation that spanned between $x_{Li} ≈ 0.9$ and ≈0.4. Physics-based simulations were then conducted to determine the role of fundamental electrochemical processes in generating this rapid delithiation behavior, which showed that this behavior is due to a significant increase in i_0 covering several

A. Grenier, K. W. Chapman
Department of Chemistry
Stony Brook University
100 Nicolls Road, Stony Brook, NY 11794, USA
J. Wang
Harbin Institute of Technology
92 Xida St, Nangang, Harbin, Heilongjiang China

2300895 (2 of 12)

**ADVANCED
SCIENCE NEWS**

www.advancedsciencenews.com

**ADVANCED
ENERGY
MATERIALS**

www.advenergymat.de
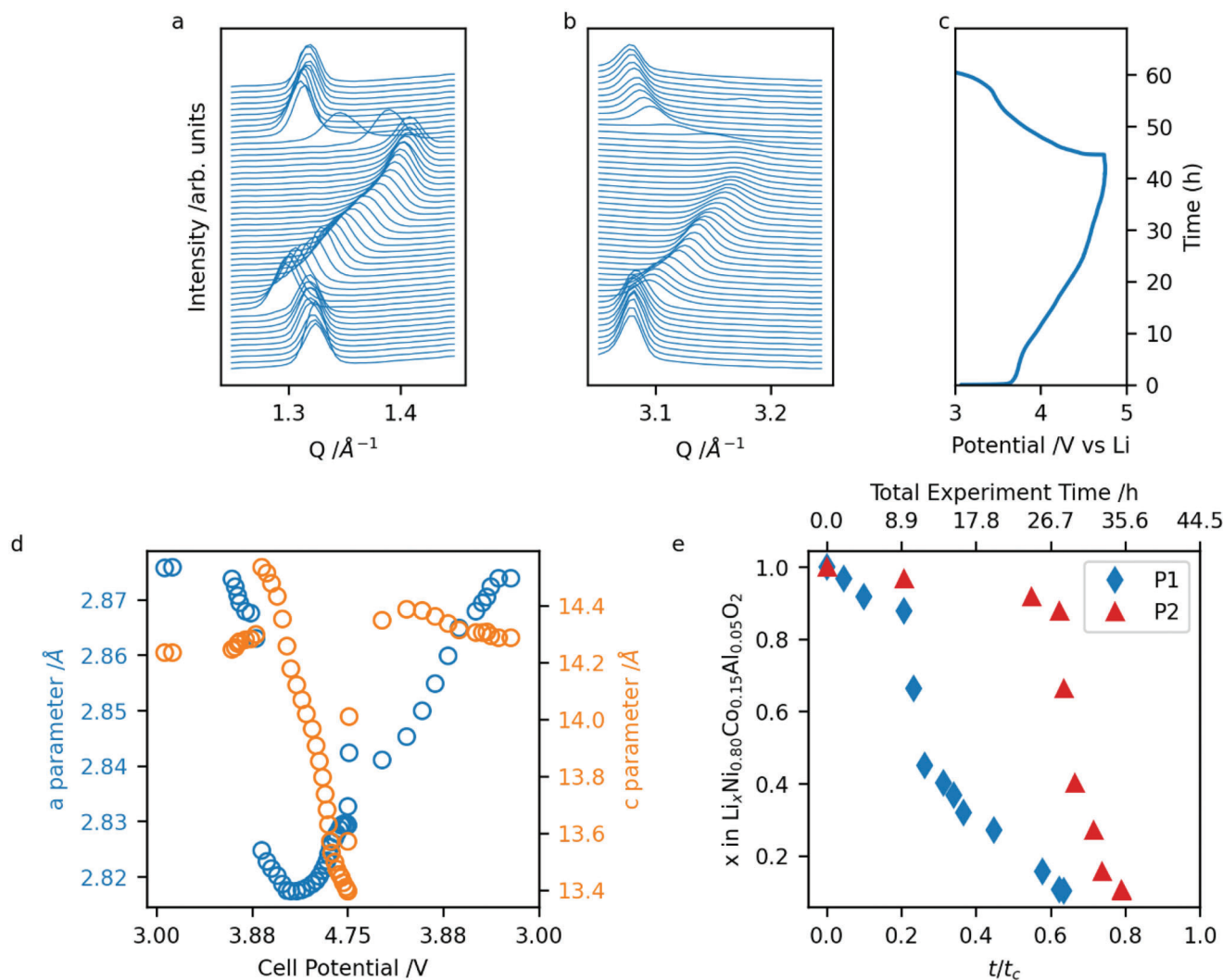
Figure 1. Operando μ-XRD of LiNi$_{0.8}$Co$_{0.15}$Al$_{0.05}$O$_2$ secondary particle agglomerates during first charge and discharge. Diffraction peaks corresponding to a) (003) and b) (104) reflections. c) Galvanostatic charge/discharge profile. d) a and c lattice parameters for a single secondary particle, P1, refined by Le Bail method. e) Extent of (de)lithiation corresponding to refined cell parameters[8] for two secondary particle agglomerates.

orders of magnitude during delithiation. These observations highlight the dissimilarity between single-particle dynamics and the macroscopic response in battery electrodes even when they follow mechanisms of solid solution. The identification of i_0 as the controlling parameter in these materials redirects models away from a focus on mass diffusion.

2. Operando Observations of Single Particle Dynamics

Secondary particles of LiNi$_{0.8}$Co$_{0.15}$Al$_{0.05}$O$_2$ were tracked during their first charge and discharge using operando μ-XRD mapping (**Figure 1**). Dilute (20 % w/w) LiNi$_{0.8}$Co$_{0.15}$Al$_{0.05}$O$_2$ electrodes were used to isolate the response of individual particles from each other. The introduction of large amounts of carbon black to dilute the particles had the beneficial effect of ensuring that the elec-

tronic conductivity of the electrode was not limiting, but it contributed to the faradaic processes on charge due to irreversible interactions with the electrolyte,[17] artificially extending the charging process (Figure 1c). For each X–Y mapping position, the individual 2D diffraction signals were integrated to one-dimensional patterns and converted from angular domain (2θ) to the momentum transfer ($|\vec{q}|$) domain, which, in turn, relates to the d spacing between planes in the crystal lattice through $d = \frac{2\pi}{|\vec{q}|}$. While data were collected with ≈500 nm spatial resolution, smaller than the particle agglomerates, all patterns from the same particle agglomerate at a given time stamp during the reaction were summed for the analyses presented here (Figure 1a,b and Figure S21, Supporting Information), to focus the analysis on the particle, rather than domain, dynamics. In all cases, the pristine state matched the literature results for LiNi$_{0.8}$Co$_{0.15}$Al$_{0.05}$O$_2$,[18] with the exception of an extra feature at $|\vec{q}| \approx 3.6$ Å^{-1} due to metallic Li

2300895 (3 of 12)

ADVANCED
SCIENCE NEWS
www.advancedsciencenews.com

ADVANCED
ENERGY
MATERIALS
www.advenergymat.de

(PDF #00-001-1131). Small extraneous peaks occurred due to random aberrations in individual pixels on the diffraction detector (Figure S21).

During (de)lithiation, the diffraction peaks for particle 1 (P1) began to shift in $|\vec{q}|$ soon after the onset of oxidation (Figure 1a), following the same overall trajectory as reported for the ensemble average.[8] This similarity and the absence of peak splitting indicates that individual particles followed a single phase mechanism, with no fictitious phase separation induced by surface impurities.[11] The most characteristic changes can be observed at the (003) and (104) reflections. The former showed an initial decrease in $|\vec{q}|$ (higher d spacing) (Figure 1a), followed by a sudden increase in $|\vec{q}|$ beyond the initial state, representing an expansion then contraction along the c axis during delithiation.[8] The (104) diffraction peak gradually shifted to higher $|\vec{q}|$ (lower d) upon removal of Li (Figure 1b), reflecting the balance between the trend along c, which is pseudo-parabolic, and the continuous decrease in the a dimension.[8] While the changes in the diffraction pattern of particle 2 (P2) covered a similar range of peak positions (Figure S21b, Supporting Information) to P1, the peaks did not begin shifting until the electrochemical cell had reached a higher potential ≈ 4.5 V. However, during subsequent lithiation the peaks in the diffraction patterns for both P1 and P2 shifted to lower $|\vec{q}|$ at approximately the same time and rate.

The evolution of the lattice parameters for each particle as a function of cell potential were extracted from refinements of the diffraction patterns (Figure 1d and Figure S23, Supporting Information). Both particles exhibited lattice parameters at the end of charge and discharge consistent with full delithiation and relithiation, respectively.[18] The trends followed by the lattice parameters during the reaction again agreed with measurements of the ensemble average in the literature,[18,19] but their timing with respect to the experiment differed. The lattice parameters for P1 began shifting at cell potentials between 3.0 V and 3.8 V and for P2 at ≈ 4.5 V (Figure 1d). All in all, the rates of change in lattice parameter for individual particles were different from the electrochemical response collected for the whole electrode. Both P1 and P2 achieved the same lattice parameters at the end of the charge sequence, observed in Figure 1e and by the peak positions in Figures 1a,b and S22.

Further insight into rates of delithiation of each particle during the reaction was extracted from the relationship between x_{Li} in $Li_xNi_{0.8}Co_{0.15}Al_{0.05}O_2$ and lattice parameters collected with PXRD in the literature[8] (Figure S21, Supporting Information). Figure 1e shows the Li content obtained from the c lattice parameter at selected time stamps for each of the two $Li_xNi_{0.8}Co_{0.15}Al_{0.05}O_2$ particles during the first charge–discharge cycle. Similar trends were observed when calculating the Li content using the a parameter (Figure S24, Supporting Information). In these plots, to allow for an easier comparison between experiments and simulation, the Li content was plotted against the ratio of time passed since current was applied to the total time to reach the charge cutoff potential (t_c), given the decoupling between the macroscopic rate of the experiment and that of individual particles. Since the experiment was performed at constant current, cumulative charging time is analogous to the extent of delithiation of the whole electrode.

Quantifying the evolution of Li content in secondary particles is a unique capability of µ-XRD, and adds new important insight

to literature observations by powder X-ray diffraction (i.e., averaging at the ensemble) and spectromicroscopy.[3–16] For both P1 and P2, the rates of delithiation, estimated from the slopes in Figure 1e, were initially low, proceeding at ≈ 0.025 Li h^{-1}, or C/40. Once the overall content of the particle reached $x_{Li} = 0.9$, the reaction dramatically accelerated nearly tenfold, to ≈ 0.3 Li h^{-1}, or C/3, until an average composition $x_{Li} = 0.4$, followed by renewed deceleration, to 0.1 Li h^{-1}, or C/10, leading to a rather small change in Li fraction until the sign of the current was reversed. In the case of P2 there was very little delithiation until 0.8 t_c. However, once it began rapid delithiation, the Li fraction evolved in a similar manner as P1, with a 20-fold acceleration at $x_{Li} = 0.9$ to ≈ 0.66 Li/h, or C/1.5 (Segments III and IV in Figure S24a,b, Supporting Information), which lasted until an average particle composition $x_{Li} = 0.$, after which the rate fell below 0.1 Li h^{-1}, or C/10, for the remainder of the delithiation process. The divergence in charging rates during a galvanostatic experiment has been recently reported by others using optical microscopy.[14] However, our ability to relate specific signatures with Li content using its well-established dependence on d spacing allows us not only to pinpoint that the rate acceleration happens at specific points of the reaction (between $x_{Li} = 0.9$ and $x_{Li} = 0.4$), but also estimate the actual rate of the process at each stage.

Upon discharge of the cell, i.e., after 1.0 t_c, both particles relithiated quickly at the initial stages, with the consequence that fewer data points were captured. Nonetheless, the lattice parameters of both particles returned to values close to the pristine state, indicating degrees of reversibility comparable to the literature.[8] When the lattice parameters reached values corresponding to $x_{Li} = 0.8$, the rates were estimated at ≈ 0.025 Li h^{-1}, or C/40. The change in the lattice parameters was smoother during discharge than during charge, with no obvious evidence of acceleration. It is worth noting that, while the end values were similar, the trajectories of both a and c parameters were not quantitatively the same as during the first charge. For instance, the c parameter peaked at 14.48 Å and 14.35 Å on charge and discharge, respectively (Figure 1d). This evolution suggests that full delithiation introduces irreversible structural changes that affect the dependence of lattice parameters on Li content. To the best of our knowledge, this issue has not been explored in the literature and demands dedicated operando PXRD experiments.

A second set of independent experiments was pursued to evaluate the reproducibility of the varying delithiation rates observed among particles by the operando µ-XRD mapping. In particular, we employed operando TXM XAS of $LiNi_{0.8}Co_{0.15}Al_{0.05}O_2$ secondary particles during charging to probe Ni oxidation states at high spatial resolution. The frames collected during these measurements were 2D projections through the particles, since the geometry of coin-cells does not permit the range of angles needed to image the particles in three spatial dimensions. Framesets containing multiple particles were collected during the first galvanostatic charge (**Figure 2**a). Localized XAS K-edge spectra were averaged over all pixels in a single secondary particle. While fractures within the secondary particle microstructure are expected at high states of charge,[20] these fractures represent movement of transition metals within the particle and so are not expected to directly effect the whole-particle spectra presented here. XAS
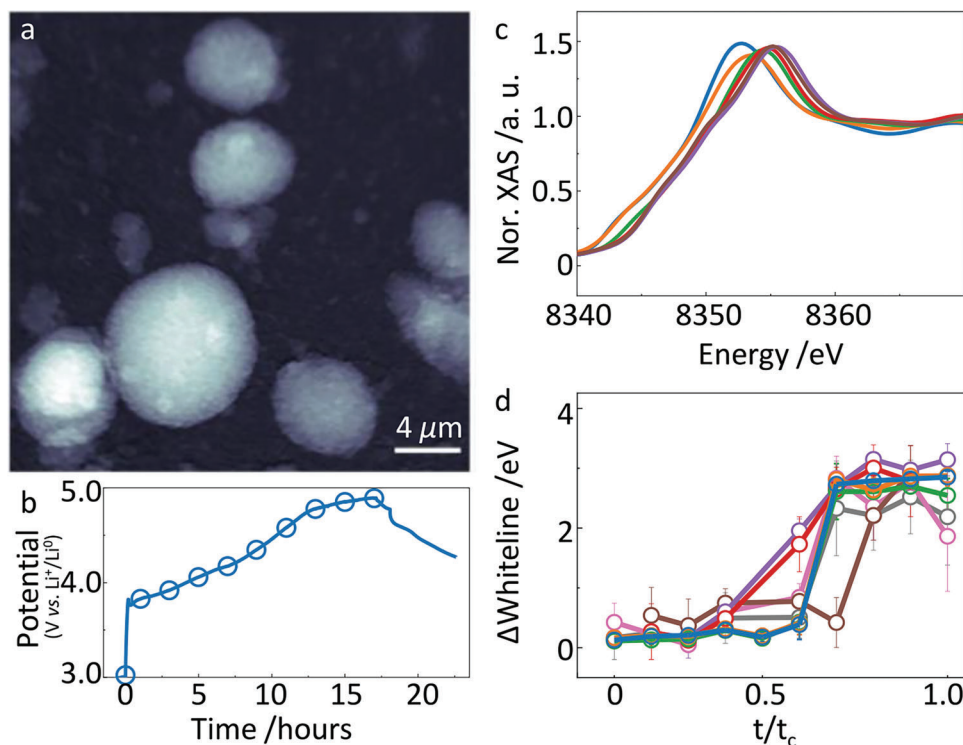
Figure 2. Operando TXM of $LiNi_{0.8}Co_{0.15}Al_{0.05}O_2$ during first charge. a) Mean optical depth frame of $LiNi_{0.8}Co_{0.15}Al_{0.05}O_2$ particles. b) Applied potential to operando cell during galvanostatic charging at 0.05 A A^{-1} h^{-1} (C/20). c) Normalized spectra from *ex-situ* ensemble-average XAS. d) State-of-charge determined by whiteline position relative to overall state of charge in (c) for individual particles of $LiNi_{0.8}Co_{0.15}Al_{0.05}O_2$. Δ is determined by the change in the energy of maximum absorbance of all pixels in a particle at a given time point relative to the energy of maximum absorbance for all particles in the pristine state. Error bars represent one standard deviation over pixels within the given particle. The horizontal axis in (d) shows the ratio of time since current was applied (t) to the total time to reach the cut-off potential (t_c).

measurements of the ensemble average of electrodes showed that, upon delithiation, there was a progressive increase in the energy of the absorption edge and the associated energy of maximum absorbance, or whiteline (Figures S12 and S13), consistent with literature observations of Ni^{2+} oxidation to Ni^{4+}.[21,22] Therefore, the whiteline energy was used as a proxy for Ni oxidation, which is the dominant redox process in $LiNi_{0.8}Co_{0.15}Al_{0.05}O_2$ and $LiNi_yMn_zCo_{1-y-z}O_2$. Figure 2c shows the changes in ensemble-average Ni K-edge XAS spectra for $LiNi_{0.8}Co_{0.15}Al_{0.05}O_2$ across known states of delithiation; these spectra were used as calibration data for the in-situ experiments. The resulting plots of average state-of-charge for each particle as a function of time are shown in Figure 2d.

Initially, the mean whiteline energies of the particles studied did not change, indicating no Ni oxidation. Between 0.4 t_c to 0.6 t_c, the whiteline energies increased rapidly for all particles, reaching 75 % to 100 % of the shift observed by ensemble XAS after first charge (Figure 2c). Although several particles oxidized concurrently, there was no clear preference for when particles began rapid oxidation. The analysis produced instances where the trend in whiteline appeared to shift toward lower energy upon reaching their maximum state-of-charge (Figure 2d), suggesting Ni reduction may have occurred, presumably due to the instability of Ni in high oxidation states,[23] resulting in oxygen loss. Overall, the observation of rapid particle oxidation despite the constant

current applied to the cell was in agreement with μ-XRD above (Figure 1).

3. Relevance to Other Cathode Materials

To evaluate the similarity between the oxidation behavior of $LiNi_{0.8}Co_{0.15}Al_{0.05}O_2$ and other layered cathode compositions, similar TXM XAS experiments were performed on cells containing dilute $LiNi_{1/3}Mn_{1/3}Co_{1/3}O_2$ and $LiNi_{0.5}Mn_{0.3}Co_{0.2}O_2$ layered cathodes (**Figure 3**). We note that $LiNi_yMn_zCo_{1-y-z}O_2$ particles (Figure 3a) were less spherical in shape as compared to $LiNi_{0.8}Co_{0.15}Al_{0.05}O_2$ (Figure 2a). The mean optical depth for all foreground pixels in the frame was used for evaluating overall oxidation (Figures 3b,c). As expected, $LiNi_{1/3}Mn_{1/3}Co_{1/3}O_2$ exhibited a lower initial whiteline energy than $LiNi_{0.8}Co_{0.15}Al_{0.05}O_2$,[21,22] matching the contrast between Ni^{2+} and Ni^{3+}. Similar to $LiNi_{0.8}Co_{0.15}Al_{0.05}O_2$, spectra for both $LiNi_yMn_zCo_{1-y-z}O_2$ cathodes showed an increase in the whiteline energy, which is in agreement with the literature.[21] To estimate the state of charge, the evolution of the whiteline was compared to the lowest value observed for any particle in the field of view during the operando experiment, reported here as Δ. For both $LiNi_yMn_zCo_{1-y-z}O_2$ materials, the same initial latent phase and subsequent rapid oxidation were seen (Figures 3d,e). The initial rapid Ni oxidation resulted in changes in whiteline

2300895 (5 of 12)

**ADVANCED
SCIENCE NEWS**

www.advancedsciencenews.com

**ADVANCED
ENERGY
MATERIALS**

www.advenergymat.de
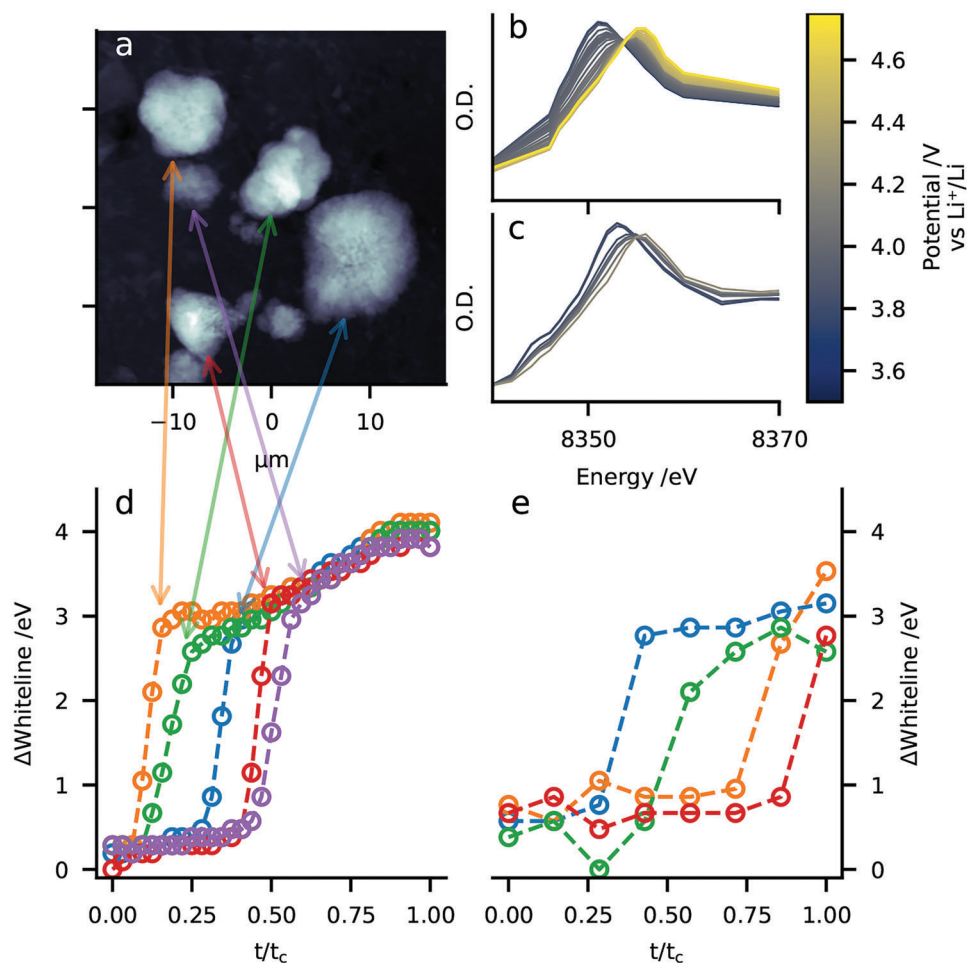
Figure 3. Operando TXM XAS of $LiNi_{1/3}Mn_{1/3}Co_{1/3}O_2$ and $LiNi_{0.5}Mn_{0.3}Co_{0.2}O_2$ during first charge. a) Mean optical depth frame of $LiNi_{1/3}Mn_{1/3}Co_{1/3}O_2$ particles. b,c) Median optical depth spectra of active material during b) second charge of $LiNi_{1/3}Mn_{1/3}Co_{1/3}O_2$ and c) first charge of $LiNi_{0.5}Mn_{0.3}Co_{0.2}O_2$. d,e) Changes in median whiteline energies during first charge relative to start of charging for individual particles of d) $LiNi_{1/3}Mn_{1/3}Co_{1/3}O_2$ and e) $LiNi_{0.5}Mn_{0.3}Co_{0.2}O_2$. Arrows show correspondence between particles in (a) and lines in (d). ΔD determination matches that described in Figure 2.

energy for $LiNi_{1/3}Mn_{1/3}Co_{1/3}O_2$ of ≈ 3 eV and $LiNi_{0.5}Mn_{0.3}Co_{0.2}O_2$ of ≈ 2.5 eV, reflecting the lower starting concentration of Ni^{2+} in $LiNi_{1/3}Mn_{1/3}Co_{1/3}O_2$. The experiment using $LiNi_{0.5}Mn_{0.3}Co_{0.2}O_2$ did not reach the same overall state of charge as those using $LiNi_{1/3}Mn_{1/3}Co_{1/3}O_2$ and $LiNi_{0.8}Co_{0.15}Al_{0.05}O_2$ due to loss of stored electron beam at the synchrotron after the particle underwent rapid delithiation. For $LiNi_{1/3}Mn_{1/3}Co_{1/3}O_2$, once rapid oxidation had occurred, a subsequent gradual increase to 4.1 eV was observed, consistent with the final phase of slower delithiation observed for NCA using μ-XRD. The total change in whiteline energy for all observed secondary particles was >4 eV (Figure 3d).

In summary, all layered cathode chemistries studied here exhibited individual secondary particles undergoing rapid delithiation at various times during galvanostatic delithiation. This behavior was observed experimentally by two independent mapping techniques (μ-XRD and TXM), with very different energies of the X-ray beam (≈ 8 keV for TXM vs 25 keV for μ-XRD). The persistence of the phenomena suggests that the behavior is inherent to layered cathode materials rather than being an artifact of the techniques, and is consistent with previous reports using

other techniques on related $LiNi_yMn_zCo_{1-y-z}O_2$ and $LiCoO_2$ layered materials.[13,15,16]

4. Simulation of Charging Dynamics

Our μ-XRD experiments clearly show that changes in rate of delithiation occur at similar Li contents in the particles, suggesting that the fundamental electrochemical properties are strongly dependent on the state of charge. While the observed phenomenon of accelerated delithiation is reminiscent of the interparticle phase separation predicted in Li_xFePO_4,[24,25] it does not apply here because the system under investigation does not permit two-phase co-existence in thermodynamic equilibrium. To understand the origin of the observed accelerated delithiation, we performed physics-based particle-level simulations of $Li_xNi_{0.8}Co_{0.15}Al_{0.05}O_2$. While the computational expense (resulting from large changes in properties with varying x) does not allow a parametric study of many-particle simulations, it was sufficient to consider 8 particles with diameters ranging from 4 μm to 11 μm in the cathode and a thin Li metal layer as the anode

**ADVANCED
SCIENCE NEWS**

www.advancedsciencenews.com

**ADVANCED
ENERGY
MATERIALS**

www.advenergymat.de
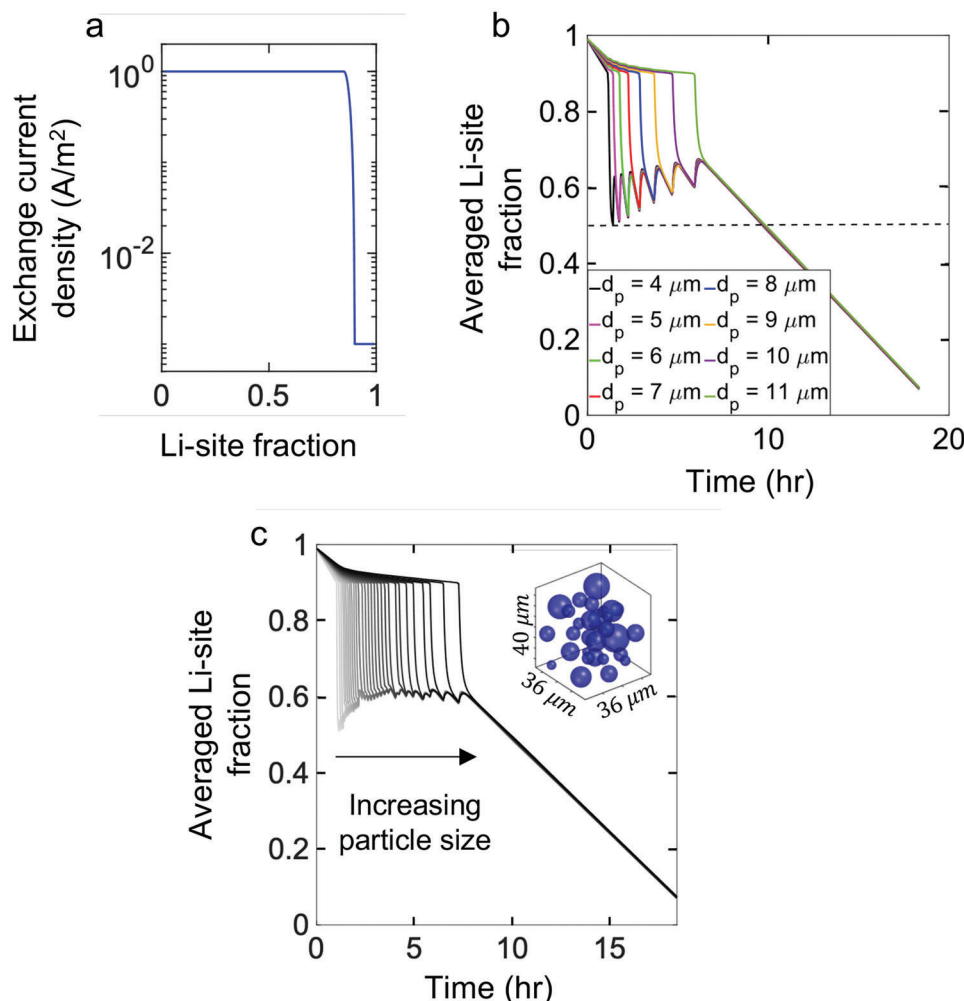
Figure 4. a) The model form of the exchange current density (i_0) versus the local Li-site fraction (x_{Li}) used for the simulation with a composition-dependent i_0. b) The simulated evolution of the volume-averaged Li-site fraction in individual particles, $\langle x_{Li} \rangle$, for C/20 galvanostatic charging of the 8-particle system. c) The simulated evolution of the volume-averaged Li-site fraction in individual particles, $\langle x_{Li} \rangle$, for C/20 galvanostatic charging of the 30-particle system.

to survey the parameter space and support the finding with one larger (30-particle) simulation. More details on the model geometry, equations, and parameters are provided in the Simulations portion of the Experimental Section and the Supporting Information.

The effect of the electrochemical reaction that occurs at the interface between the active material and the electrolyte phase can be studied by varying the exchange current density (i_0). Similarly, the effect of the solid-state transport can be studied by examining the coefficient of Li diffusivity in particles (D_s). Both of these quantities are dependent on the local Li-site fraction (x_{Li}) within the particles. Therefore, we performed sensitivity analyses with respect to various functional forms and values of i_0 and D_s, including those in literature[13,20,26–34] and those constructed for this work to qualitatively reproduce rapid delithiation. Note that we use the value of x_{Li} at each point in the discretized space, rather than the volume averaged values over a particle, to determine the local values of i_0 and D_s in simulations in which functional forms are used. Thus, the spatial variations in these parameters are ac-

counted for in the simulations. Further details of these forms are provided in the Supporting Information.

Figure 4b shows the evolution of volume-averaged Li-site fraction, $\langle x_{Li} \rangle$, of the 8 particles for 0.05 A A^{-1} h^{-1} (C/20) charging obtained using a model form of i_0 that was constructed based on the recent studies of LiNi$_{0.8}$Co$_{0.15}$Al$_{0.05}$O$_2$[13] and LiNi$_y$Mn$_z$Co$_{1-y-z}$O$_2$.[20,32,33] Figure 4a shows the dependence of the model form of i_0 on x_{Li} that exhibited rapid delithiation similar to the experiment. The model i_0 is a smoothed step function with a significant increase in the value with decreasing x around a transition point ($x_{Li} \approx 0.9$). As can be seen in Figure 4b, all the particles exhibit rapid delithiation. When a particle reaches $\langle x_{Li} \rangle \approx 0.9$, i_0 begins to increase rapidly and thereby causes the particle to experience an accelerated reaction rate as it is further delithiated. This acceleration causes the particle to contribute the majority of the applied current, which stagnates the delithiation rate of other particles that have not reached the transition point under galvanostatic conditions. By the time the particle completes its accelerated delithiation, another particle

**ADVANCED
SCIENCE NEWS**

www.advancedsciencenews.com

**ADVANCED
ENERGY
MATERIALS**

www.advenergymat.de
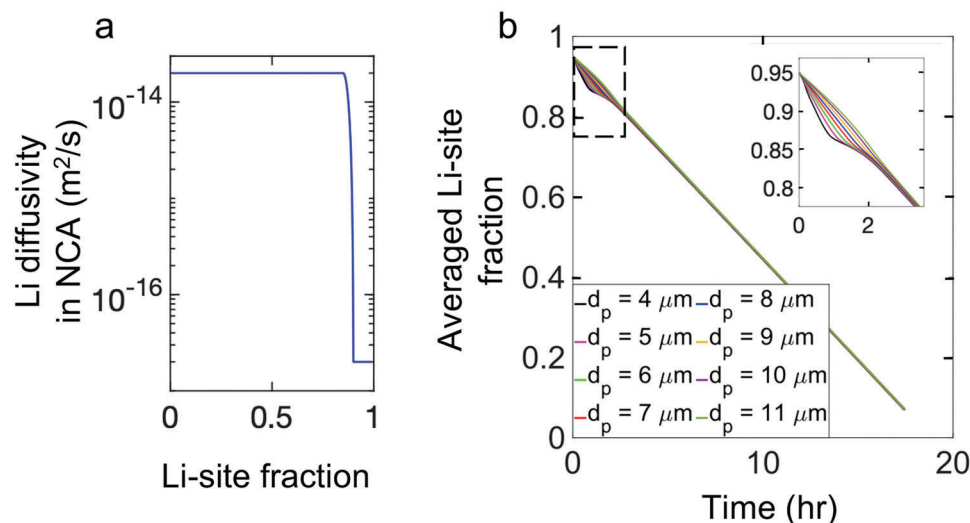
Figure 5. a) The model form of D_s, vs. the local Li-site fraction (x_{Li}) used for the simulation with a composition-dependent diffusivity. Note that the form of the function is the same as that of i_0 shown above, including the ratio between the maximum and minimum values and the width of the transition. b) The simulated evolution of the volume-averaged x_{Li} in individual particles, $\langle x_{Li} \rangle$, for C/20 galvanostatic charging of the 8-particle system. The inset shows the magnified view of the section bounded by the dashed box.

undergoes this transition and thus rapid delithiation. This cycle repeats until the last particle undergoes rapid delithiation. We note that no rapid delithiation was observed when the traditional form of i_0 ($\propto \sqrt{x_{Li}(1 - x_{Li})}$) is used,[28,31,35,36] as shown in Figure S6 (Supporting Information). The oscillations observed in $\langle x_{Li} \rangle$ in Figure 4b arise due to the large difference between minimum and maximum values of i_0 used in these simulations. This large difference can cause a particle undergoing the aforementioned transition to deliver more than the applied current, which induces already delithiated particles to lithiate slightly. This mechanism is different from the similar phenomena observed in Li_xFePO_4, for which the acceleration occurs due to the thermodynamics of the phase-separating material.[37]

To ensure that the results from the 8-particle simulations are not artificially affected by the system size, we performed a simulation with 30 particles; the details of the simulation are provided in the Supporting Information. The results are provided in Figure 4c. First, rapid delithiation is observed for all of the particles even in a larger system, which shows that such behavior is likely intrinsic to the material. Second, the amplitudes of the oscillations decrease in the simulation with 30 particles as compared to the 8-particle system, which suggests that oscillations may not occur in very large systems such as practical electrodes. Confirming whether or not such oscillations in state of charge occur in a physical system would require higher chemical and temporal resolutions than what is possible with these techniques today.

Next, we studied the effect of the function form of D_s by employing the same form as the model i_0 above, as shown in **Figure 5**a. Note that the traditional form of i_0 was used for this simulation, and initial $\langle x_{Li} \rangle$ is set to 0.95 instead of 0.99 in this simulation to avoid unphysical situations such as $\langle x_{Li} \rangle > 1$, which can arise from a numerical error caused by a rapid change in D_s with respect to x_{Li}. Figure 5b shows the evolution of $\langle x_{Li} \rangle$ during charging of the 8-particle system at 0.05 A A^{-1} h^{-1} (C/20)

with the model D_s. Although accelerated delithiation is observed for smaller particles, its extent is much smaller than that observed due to the change in i_0, discussed above. For a particle to exhibit rapid delithiation, the flux at the particle-electrolyte interface needs to increase rapidly in a short duration of time. Such an increase in the flux cannot be realized even if the diffusion function has a step-function-like dependence on x_{Li} because the diffusivity (hence, diffusion flux) only increases in the outer shell of the particle; the particle bulk continues to have lower diffusivity. In other words, the entire particle does not undergo rapid delithiation; instead, only the outer shell exhibits such behavior. Furthermore, prior results do not show a preference for delithiation at the outside of the particles[38], as would be expected if Li transport was sluggish, suggesting that Li diffusion is not the limiting mechanism in these experiments. Indeed, the simulation result also supports this conclusion for the values of D_s obtained from the literature, as well as the step form of D_s having a 1000-fold smaller value. Hence, we can rule out a strong dependence of D_s on x_{Li} as the underlying cause of rapid delithiation.

Based on the insights generated above, we conclude that rapid delithiation in $LiNi_{0.8}Co_{0.15}Al_{0.05}O_2$ particles is controlled by the surface reaction kinetics, rather than the bulk Li diffusion dynamics in the active material. This result from our deterministic modeling study agrees well with the stochastic simulations performed by Park et al.,[13] where the authors showed that the accelerated delithiation (termed electro-autocatalysis by the authors) is controlled by the surface reaction and not the solid-state diffusion. Moreover, the authors reported a rapid increase in i_0 at the $LiNi_{0.8}Co_{0.15}Al_{0.05}O_2$ particle surface as the delithiation progresses, albeit with a different form of the function. The authors used an exponential relation between i_0 and x_{Li}, while we used a smoothed-step function.

Electrode morphology above the length-scale of secondary particles has been shown to affect lithiation kinetics in electrodes

prepared with layered cathode material.[14,39–41] We note that the electrodes used in our experimental TXM measurements were prepared with a high carbon-additive content (60% w/w), and thus ensured minimal spatial inhomogeneity in the electrostatic potential throughout their volume. Rapid delithiation was observed regardless of carbon and binder loading (Figures 1–3), as well as when using dense, thin electrodes[13] where transport through the electrode is not predicted to be limiting.[40] Therefore, experimental observations of rapid delithiation in such electrodes suggest that the behavior is governed by material properties rather than electrode morphology. However, electrode morphology likely still contributes to the inter-particle dynamics. While this mechanism implies a driving force for inter-particle heterogeneity during cycling,[13] limited electronic conductivity and/or Li+ transport will require some particles to reach higher over-potentials than others before undergoing the rapid increase in exchange current density. Particles observed during rapid delithiation (Figures 2 and 3) showed a larger change in white-line energy, and thus a higher extent of nickel oxidation, than that seen in ensemble-average experiments (Table S2, Supporting Information), indicating that it is possible for these particles to reach full delithiation even in composite electrodes. This implies that a portion of the secondary particles in the electrode do not oxidize during first charge, as can be seen for particle 3 in our μ-XRD results (Figure S21c, Supporting Information). More deliberate design of the electrode structure may therefore result in higher utilization of active material. Given that the step change in i_0 happens over a narrow compositional domain at high Li contents ($x \approx 0.9$ in Li$_x$MO$_2$), cycling electrodes in a way that avoids full relithiation would naturally induce cycling within the high i_0 domain and prevent this kinetic effect, at the expense of a capacity penalty.

Several studies have attributed the rapid delithiation to limited diffusion of Li in the cathode active material,[15,16] rather than changes in exchange current density. Their models and those described above (our model with the step form of D_s and the model presented by Park et al.[13]) predict spatial heterogeneity within secondary particles in the diffusion limited case.[16] However, no such spatial heterogeneity is experimentally observed in the polycrystalline secondary particles, neither in this work nor that of other authors.[13,14] This difference between polycrystalline and single crystal cathode behavior implies that Li diffusion may be the limiting factor in the case of large single crystal particles, but that polycrystalline secondary particles are instead limited by charge-transfer kinetics.

5. Conclusion

Operando X-ray characterization of layered cathode materials showed rapid and stochastic oxidation within the cathode at the level of secondary particle agglomerates. This behavior was consistent across cathodes with several transition metal compositions, and when measured by two distinct X-ray characterization modalities. The robustness with which this effect was measured demonstrates it to be inherent to layered cathode materials. By leveraging the unique insight from μ-XRD into lattice spacing and Li content, a 10-to-20-fold acceleration of the rate of delithiation was found at $x_{Li} \approx 0.9$, until ≈ 0.4. Subsequent modeling of the electrochemical dynamics showed the origins of this

rapid delithiation to be the result of a dramatic increase in the i_0 value at these Li contents. Rapid stochastic delithiation explains the apparent two-phase behavior reported by conventional PXRD: it is an emergent property resulting from the ensemble-average nature of the technique rather than being inherent to the thermodynamics of layered cathode materials. The spectro-microscopy results presented here reveal that individual particles can reach a higher state of charge than the global average during cycling, highlighting the heterogeneity within the electrode and the need for experimental techniques such as those applied here that provide spatial, temporal and chemical resolutions. These factors present areas of improvement for the performance of layered cathode materials, which could be realized with further research into the origin of the significant increase in i_0 during charging.

6. Experimental Section

μ-XRD Mapping: The LiNi$_{0.8}$Co$_{0.15}$Al$_{0.05}$O$_2$ composite electrode tape was cast in a dry room (dew point of <-35 °C) using the Bellcore method.[42] A mixture of LiNi$_{0.8}$Co$_{0.15}$Al$_{0.05}$O$_2$, poly(vinylidene fluoride-co-hexafluoropropylene) (PVDF-HFP, Kynar 2801, Elf Atochem), carbon black (Super P, MMM), propylene carbonate (Aldrich), and acetone (Aldrich) was used for the casting slurry. After casting, the tape was allowed to dry in air, and then the propylene carbonate plasticizer was extracted by soaking the tape in 99.8% anhydrous diethyl ether (Aldrich). The electrode tape had a mass composition of 20% active material, 20% carbon additive, and 60% binder. Prior to storage in the Ar-filled glovebox, the tape was dried under vacuum at 120 °C overnight.

The AMPIX electrochemical cell was utilized to allow X-ray penetration through the electrode.[43] Lithium metal was used as the counter electrode and the electrolyte was composed of 1M LiPF$_6$ in a 1:1 mixture of ethylene carbonate:dimethyl carbonate. Glass fiber served as the separator.

Diffraction maps were collected using the microprobe beamline at beamline 34-ID-E at the Advanced Photon Source, Argonne National Laboratory (APS). An incoming monochromatic beam at 25 keV (0.4959 Å) with a size of 0.5 μm was shone through the AMPIX cell onto the sample. The intensity of the diffracted beam was collected in transmission geometry by a MAR165 CCD detector, with 4096 pixels, each measuring 40 μm^2, used in 2 binning mode.

Particle locations were determined through absorption contrast imaging over the Ni K$_\alpha$ emission line at ≈8 keV. Once particles were located, the sample was moved relative to the beam using a step size of 1 μm and an exposure time of 10 s. 2D diffraction maps were collected in this manner continuously over the charge-discharge cycle. At each exposure, or mapping position, a single full 2D diffraction pattern, averaging over the depth of the material, was collected (an example is shown in Figure S10, Supporting Information). Maps of the summed diffraction intensity for each particle at open-circuit conditions are shown in Figure S11a–c (Supporting Information). After one map was collected for each particle, a positive current was applied so that the charge rate would be C/20 (in which removal of a full Li equivalent would complete in 20 h). The cut-off potential for the cell was set for 4.8 V, to ensure a complete oxidation of the LiNi$_{0.8}$Co$_{0.15}$Al$_{0.05}$O$_2$. After holding the cell near 4.8 V for several hours, the cell was discharged at a negative current equal in magnitude to that of the charge. The data were collected using EPICS channel-access data acquisition and control software.

The 2D diffraction data collected by the beamline was integrated using the FIT2D software package developed by ESRF.[44,45] The integrated data was processed with the Scimap analysis package,[46] in which the determination of the peak position yielded a set of unit cell parameters for each mapping position, which were plotted using Python. An ensemble diffraction pattern for each particle at each

ADVANCED
SCIENCE NEWS

www.advancedsciencenews.com

ADVANCED
ENERGY
MATERIALS

www.advenergymat.de

state of charge was obtained by summing the patterns at each mapping position. These patterns underwent batch Le Bail refinement by the TOPAS software developed by Bruker to produce plots of unit cell as a function of charge-discharge for each particle as a whole (Figure S11d-e).

Ex-situ X-ray Absorption Spectroscopy - LiNi$_{0.8}$Co$_{0.15}$Al$_{0.05}$O$_2$: To obtain standard spectra of LiNi$_{0.8}$Co$_{0.15}$Al$_{0.05}$O$_2$ (NAT-1050) with respect to the states-of-charge, dense composite electrodes were fabricated by mixing the pristine LiNi$_{0.8}$Co$_{0.15}$Al$_{0.05}$O$_2$ with acetylene black and polyvinylidene difluoride (PVDF) in 80:10:10 ratio in N-methylpyrrolidone. The resulting slurry was cast onto a pre-weighed Al foil disk, dried at room temperature, followed by a heat treatment of 120 °C under vacuum for 12 h. The composite electrodes were assembled in two-electrode 2032 coin cells using lithium foil as both counter and pseudo-reference electrode, and Celgard 2400 separator soaked in a 45:55 mixture of ethylenecarbonate and dimethyl carbonate containing 1 M LiPF$_6$ as electrolyte. All cell assembly and sample manipulation was performed in an Ar-filled glovebox. Galvanostatic cycling at a 0.05 A A^{-1} h^{-1} (C/20) rate (defined as the current density for full delithiation of LiNi$_{0.8}$Co$_{0.15}$Al$_{0.05}$O$_2$ in 20 h) was performed between 3.0 V to 4.8 V vs. Li$^+$/Li^0 using a Bio-Logic VSP potentiostat/galvanostat. The reference powders for LiNi$_{0.8}$Co$_{0.15}$Al$_{0.05}$O$_2$ were harvested from Li metal half cells charged to specific state-of-charges (25 %, 50 %, 75 %, and 100 %) and heat-sealed in polyethylene to minimize O$_2$ and H$_2$O exposure. Ni K-edge XAS transmission spectra were collected for the discrete states of charge and the pristine state at beamline 4-1 at the Stanford Synchrotron Radiation Lightsource (SSRL), in transmission mode using a Si (220) double crystal monochromator (Figure 2c). A Ni metal standard foil located in front of a reference ion-chamber was measured simultaneously with each spectral sample for energy calibration. All data processing, including normalization of transmission spectra was carried out using the software SIXPACK.[47] Pre-edge background subtraction and X-ray absorbance near edge spectroscopy (XANES) normalization were carried out by fitting a linear polynomial to the pre-edge region and a quadratic polynomial to the post-edge region of the absorption spectrum. All XANES spectra were linearly calibrated using the energy threshold E_0 of the reference Ni foil determined from the first derivative peak of the spectrum.

TXM - LiNi$_{0.8}$Co$_{0.15}$Al$_{0.05}$O$_2$: To visualize the macroscopic electrochemical properties of single-isolated LiNi$_{0.8}$Co$_{0.15}$Al$_{0.05}$O$_2$ (NAT-1050) secondary powders, diluted and thinner composite electrodes were fabricated by mixing the pristine LiNi$_{0.8}$Co$_{0.15}$Al$_{0.05}$O$_2$ with acetylene black and polyvinylidene difluoride (PVDF) in 20:50:30 ratio in N-methylpyrrolidone. The resulting slurry was cast onto a pre-weighed Al foil disk with a thickness of 30 μm, dried at room temperature, followed by a heat treatment at 120 °C under vacuum for 12 h. The composite electrodes were assembled in 2032 coin cells (modified as described below) using lithium foil as both counter and pseudo-reference electrode, and Celgard 2400 separator soaked in a 45:55 mixture of ethylenecarbonate and dimethyl carbonate containing 1 M LiPF$_6$ as electrolyte. To ensure sufficient transparency to the X-ray beam, holes were punched in the cell cases. After cell assembly, the holes in the cell cases were sealed with 1 μm thick Si$_3$N$_4$ windows (Norcada NX5200F) using Torr-Seal vacuum-rated epoxy. All cell assembly and sample manipulation was performed in an Ar-filled glovebox. Operando TXM was performed at the 54 pole wiggler beamline (BL 6-2) at SSRL.[48] Galvanostatic cycling at a 0.05 A A^{-1} h^{-1} (C/20) rate was performed between 3.0 V to 5.0 V vs. Li$^+$/Li$_0$ using a Bio-Logic VMP potentiostat/galvanostat. The absorption contrast images (0.5 s exposure time, 10 repetitions, binning 2, 1024 × 1024 pixels) were captured across Ni K-edge (from 8250 eV to 8650 eV in 47 steps) with spatial and energy resolutions of ≈30 nm and $\frac{\Delta E}{E} = \approx 1 \times 10^{-4}$, respectively. In order to eliminate distortions in flux and small beam instabilities, simultaneous acquisition of reference images through an open or outside area of the sample were performed at each energy and charging state (0.5 s exposure time, 10 repetitions, binning 2, 1024 × 1024 pixels), then used for converting transmission images to optical depth (OD) images following the Beer–Lambert law. The repetitions in the exposures were performed for improving the dynamic range of the detector, thereby increasing the signal to noise ratio in the data. The chemical mapping for a single field of view was accomplished in 37 min. OD images were aligned with sub-pixel resolution by using an iterative registration method with intensity-base automatic image alignments.[49] The chemical composition of each pixel was estimated by the position of the whiteline peak, which is proportional to the state of charge (Figure S14, Supporting Information). The positions of the whiteline peaks were determined by the Gaussian fits together with 7 nearest points near the highest OD position.

TXM - LiNi$_y$Mn$_z$Co$_{1-y-z}$O$_2$: LiNi$_{1/3}$Mn$_{1/3}$Co$_{1/3}$O$_2$ (NM-3100) and LiNi$_{0.5}$Mn$_{0.3}$Co$_{0.2}$O$_2$ (NCM-045T) were purchased from TODA America, Inc. and either stored under ambient atmosphere (Figures S13, S20, S19, and S16a-d, Supporting Information) or in a dry room followed by an argon-filled glovebox (Figures S17, S16e,f, S18, and S15, Supporting Information). LiNi$_{0.8}$Co$_{0.15}$Al$_{0.05}$O$_2$ or LiNi$_y$Mn$_z$Co$_{1-y-z}$O$_2$ powder (20 %, TODA) and acetylene black (60 %) were ground in a mortar and pestle, then mixed with polyvinylidene fluoride (Solvay, 2 % in N-methyl-2-pyrrolidone) to equal 20 % of dry composite. The resulting slurry was spread onto battery grade aluminum foil using a cylindrical applicator set to 102 μm coating thickness. Electrode laminate was dried in ambient atmosphere under infrared lamp for ≈15 min and placed in vacuum oven at 110 °C overnight.

Cells for operando TXM were prepared by drilling holes of 800 μm (bottom, cathode-side), 1500 μm (top), or 3000 μm (spacer, anode-side) diameter in the centers of the corresponding coin-cell parts (2032, 316L stainless steel, Hohsen Corp.). 12.7 mm diameters cathodes were assembled in these modified coin-cell parts with 1 M LiPF$_6$ in 1:1 EC/DMC electrolyte and 12.7 mm diameter Li metal anode inside an argon-filled glovebox. Once crimped, holes in the coin-cell were covered with 1 μm thick Si$_3$N$_4$ windows (Norcada NX5200F) using Torr-Seal vacuum-rated epoxy. Assembled and sealed cells were removed from the glovebox and mounted in the X-ray microscope.

TXM was performed at the Advanced Photon Source bending magnet beamline 8-BM-B (Figures S17, S20, and S19, Supporting Information), equipped with an XRadia transmission microscope. A 60 nm outer-zone-width objective zone-plate was used to render a magnified image on a 2048 × 2048 charge-coupled device with binning factor 2, producing 1024 × 1024 intensity images.

Operando data acquisition was performed by collecting frames at each energy of both the specimen and a reference frame with no cell or sample in the field of view. Image processing was performed using the xanespy package.[50] Optical depth (OD) images were calculated from the object frame (I) and reference frame (I_0) as

$$OD = \log\left(\frac{I_0}{I}\right) \tag{1}$$

All images within a full operando experiment were aligned using multiple passes (as needed) of the `register_translation` function provided by scikit-image[51] using the mean optical-depth frame as the target image. Image normalization was performed on each frame by subtracting the median optical depth of all background pixels (determined by thresholding using Otsu's method[52]) of that frame.[53] Pixels not containing an appreciable level of Ni spectral signal were masked by calculating the ratio of the edge jump (difference between the post-edge and pre-edge optical depths) to the standard deviation of the optical depth spectrum. This ratio was calculated for the whole frame-set, then a threshold for the mask was determined using Otsu's method[52] through scikit-image.[51] Spectra for pixels passing this edge filter were then fit with a linear combination of a background line, Gaussian peak and arctangent function:

$$OD(E) = t + s\left[\frac{1}{\pi}\arctan(\sigma(E - E_0)) + \frac{1}{2} + ae^{\frac{-(E-E_0-b)^2}{2c^2}} + m(E - E_0)\right] \tag{2}$$

with fitting parameters σ to control the width of the arctangent edge jump; a, b, c to control the height, position and width of the Gaussian whiteline peak; m to control the slope of the background; E_0 to represent the absolute energy of the edge; and s, t to control the overall scale and vertical offset of the spectrum. Fitting was performed with

**ADVANCED
SCIENCE NEWS**

www.advancedsciencenews.com

**ADVANCED
ENERGY
MATERIALS**

www.advenergymat.de

the `scipy.optimize.leastsq` wrapper around the MINPACK `lmdif` routine.[54] Whiteline positions were extracted by re-sampling the above parametric function with 200 energies and selecting the energy of maximum optical depth. Plotting was performed using matplotlib.[55]

Simulations: To understand how different particles undergo the delithiation process, particle-level models were constructed based on previous work.[56] In particular, two models were considered, one with 8 particles, and another with 30 particles. The first model (8-particle) simulated the 1) transport of Li-ions in the electrolyte, 2) transport of electrons in the cathode, 3) solid-state transport of Li in the active material particles, and 4) electrochemical reaction at the active material surface. However, due to the large volume fractions of the pore phase and the carbon additive in the cathode, the effects of mechanisms (1) and (2) were ignored in the second model (30-particle). The first model was simulated using the finite elements method in COMSOL Multiphysics 5.6, and for simulating the second model, the smoothed boundary method[57] was employed together with the finite difference method in the in-house developed Fortran code. Some of the material parameters, such as the ionic diffusivity, conductivity, transference number, thermodynamic factor, and electronic conductivity of the $LiNi_{0.8}Co_{0.15}Al_{0.05}O_2$ electrode were obtained directly from the literature,[58,59] while others were either sourced from experiments or constructed for this work, as listed in Table S1 (Supporting Information) and explained in the Supporting Information. Additional details about these models such as model equations and geometry are also provided in the Supporting Information.

Supporting Information

Supporting Information is available from the Wiley Online Library or from the author.

Acknowledgements

Conflict of Interest

The authors declare no conflict of interest.

Data Availability Statement

Data from operando μ-XRD and operando TXM are available online at https://doi.org/10.17038/XSD/1987481. All other data are available from the authors upon reasonable request.

Keywords

[1] M. Bianchini, M. Roca-Ayats, P. Hartmann, T. Brezesinski, J. Janek, *Angew. Chemie Int. Ed.* **2019**, *58*, 10434.

[2] J. Liu, J. Wang, Y. Ni, K. Zhang, F. Cheng, J. Chen, *Mater. Today* **2020**.

[3] F. Lin, Y. Liu, X. Yu, L. Cheng, A. Singer, O. G. Shpyrko, H. L. Xin, N. Tamura, C. Tian, T.-C. Weng, X.-Q. Yang, Y. S. Meng, D. Nordlund, W. Yang, M. M. Doeff, *Chem. Rev.* **2017**, *117*, 13123.

[4] M. Wolf, B. M. May, J. Cabana, *Chem. Mater.* **2017**, *29*, 3347.

[5] M. van Hulzen, F. G. B. Ooms, J. P. Wright, M. Wagemaker, *Front. Energy Res.* **2018**, *6*.

[6] J. Ahn, D. Susanto, J.-K. Noh, G. Ali, B. W. Cho, K. Y. Chung, J. H. Kim, S. H. Oh, *J. Power Sources* **2017**, *360*, 575.

[7] Y.-N. Zhou, J.-L. Yue, E. Hu, H. Li, L. Gu, K.-W. Nam, S.-M. Bak, X. Yu, J. Liu, J. Bai, E. Dooryhee, Z.-W. Fu, X.-Q. Yang, *Adv. Energy Mater.* **2016**, *6*, 1600597.

[8] R. Robert, C. Bünzli, E. J. Berg, P. Novák, *Chem. Mater.* **2015**, *27*, 526.

[9] W.-S. Yoon, K. Y. Chung, J. McBreen, X.-Q. Yang, *Electrochem. Commun.* **2006**, *8*, 1257.

[10] W. Hua, B. Schwarz, M. Knapp, A. Senyshyn, A. Missiul, X. Mu, S. Wang, C. Kübel, J. R. Binder, S. Indris, H. Ehrenberg, *J. Electrochem. Soc.* **2018**, *166*, A5025.

[11] A. Grenier, H. Liu, K. M. Wiaderek, Z. W. Lebens-Higgins, O. J. Borkiewicz, L. F. J. Piper, P. J. Chupas, K. W. Chapman, *Chem. Mater.* **2017**, *29*, 7345.

[12] A. Grenier, P. J. Reeves, H. Liu, I. D. Seymour, K. Märker, K. M. Wiaderek, P. J. Chupas, C. P. Grey, K. W. Chapman, *J. Am. Chem. Soc.* **2020**, *142*, 7001.

[13] J. Park, H. Zhao, S. D. Kang, K. Lim, C.-C. Chen, Y.-S. Yu, R. D. Braatz, D. A. Shapiro, J. Hong, M. F. Toney, M. Z. Bazant, W. C. Chueh, *Nat. Mater.* **2021**, *20*, 991.

[14] N. Sharma, L. S. de Vasconcelos, S. Hassan, K. Zhao, *Nano Lett.* **2022**, *22*, 5883.

[15] A. J. Merryweather, C. Schnedermann, Q. Jacquet, C. P. Grey, A. Rao, *Nature* **2021**, *594*, 522.

[16] M. Ge, S. Wi, X. Liu, J. Bai, S. Ehrlich, D. Lu, W.-K. Lee, Z. Chen, F. Wang, *Angew. Chemie Int. Ed.* **2020**.

[17] S. F. Lux, E. Pollak, U. Boesenberg, T. Richardson, R. Kostecki, *Electrochem. Commun.* **2014**, *46*, 5.

[18] R. Robert, P. Novák, *J. Electrochem. Soc.* **2015**, *162*, A1823.

[19] N. V. Faenza, N. Pereira, D. M. Halat, J. Vinckeviciute, L. Bruce, M. D. Radin, P. Mukherjee, F. Badway, A. Halajko, F. Cosandey, C. P. Grey, A. Van der Ven, G. G. Amatucci, *Chem. Mater.* **2018**, *30*, 7545.

[20] P.-C. Tsai, B. Wen, M. Wolfman, M.-J. Choe, M. S. Pan, L. Su, K. Thornton, J. Cabana, Y.-M. Chiang, *Energy Environ. Sci.* **2018**, *11*, 860.

[21] A. Deb, U. Bergmann, S. P. Cramer, E. J. Cairns, *J. Appl. Phys.* **2005**, *97*, 113523.

[22] T. Sasaki, T. Nonaka, H. Oka, C. Okuda, Y. Itou, Y. Kondo, Y. Takeuchi, Y. Ukyo, K. Tatsumi, S. Muto, *J. Electrochem. Soc.* **2009**, *156*, A289.

[23] N. Voronina, Y.-K. Sun, S.-T. Myung, *Acs Energy Lett.* **2020**, *5*, 1814.

[24] U. Boesenberg, F. Meirer, Y. Liu, A. Shukla, R. Dell'Anna, T. Tyliszczak, G. Chen, J. Andrews, T. Richardson, R. Kostecki, J. Cabana, *Chem. Mater.* **2013**, *25*, 1664.

[25] B. Orvananos, R. Malik, H.-C. Yu, A. Abdellahi, C. P. Grey, G. Ceder, K. Thornton, *Electrochim. Acta* **2014**, *137*, 245.

[26] R. Amin, D. B. Ravnsbæk, Y.-M. Chiang, *J. Electrochem. Soc.* **2015**, *162*, A1163.

[27] R. Moshtev, *J. Power Sources* **1984**, *11*, 93.

[28] M. Doyle, T. F. Fuller, J. Newman, *J. Electrochem. Soc.* **1993**, *140*, 1526.

[29] M. Doyle, T. F. Fuller, J. Newman, *Electrochim. Acta* **1994**, *39*, 2073.

[30] M. Doyle, J. Newman, *Electrochim. Acta* **1995**, *40*, 2191.

[31] M. Doyle, J. Newman, A. S. Gozdz, C. N. Schmutz, J. Tarascon, *J. Electrochem. Soc.* **1996**, *143*, 1890.

[32] A. Verma, K. Smith, S. Santhanagopalan, D. Abraham, K. P. Yao, P. P. Mukherjee, *J. Electrochem. Soc.* **2017**, *164*, A3380.

[33] B. Wen, Z. Deng, P.-C. Tsai, Z. W. Lebens-Higgins, L. F. J. Piper, S. P. Ong, Y.-M. Chiang, *Nat. Energy* **2020**, *5*, 578.

[34] D. Abraham, S. Kawauchi, D. Dees, *Electrochim. Acta* **2008**, *53*, 2121.

[35] T. F. Fuller, M. Doyle, J. Newman, *J. Electrochem. Soc.* **1994**, *141*, 1.

[36] J. Newman, *J. Electrochem. Soc.* **1995**, *142*, 97.

[37] B. Orvananos, H.-C. Yu, R. Malik, A. Abdellahi, C. P. Grey, G. Ceder, K. Thornton, *J. Electrochem. Soc.* **2015**, *162*, A1718.

[38] L. Wang, T. Liu, A. Dai, V. D. Andrade, Y. Ren, W. Xu, S. Lee, Q. Zhang, L. Gu, S. Wang, T. Wu, H. Jin, J. Lu, *Nat. Commun.* **2021**, *12*, 1.

[39] G. Liu, H. Zheng, X. Song, V. S. Battaglia, *J. Electrochem. Soc.* **2012**, *159*, A214.

[40] A. N. Mistry, K. Smith, P. P. Mukherjee, *Acs Appl. Mater. & Interfaces* **2018**, *10*, 6317.

[41] A. Mistry, K. Smith, P. P. Mukherjee, *Acs Appl. Mater. & Interfaces* **2020**, *12*, 16359.

[42] J.-M. Tarascon, A. Gozdz, C. Schmutz, F. Shokoohi, P. Warren, *Solid State Ionics* **1996**, *86-88*, 49.

[43] O. J. Borkiewicz, B. Shyam, K. M. Wiaderek, C. Kurtz, P. J. Chupas, K. W. Chapman, *J. Appl. Crystallogr.* **2012**, *45*, 1261.

[44] A. P. Hammersley, S. O. Svensson, M. Hanfland, A. N. Fitch, D. Hausermann, *High Pressure Res.* **1996**, *14*, 235.

[45] A. Hammersley, *FIT2D: An Introduction and Overview*, **1997**.

[46] M. Wolfman, Scimap, https://github.com/canismarko/scimap/ (accessed: October 2018).

[47] S. M. Webb, I. McNulty, C. Eyberger, B. Lai, in *AIP Conference Proceedings*, Vol *1365*, AIP, Haldenwang **2011**.

[48] J. C. Andrews, S. Brennan, C. Patty, K. Luening, P. Pianetta, E. Almeida, M. C. H. van der Meulen, M. Feser, J. Gelb, J. Rudati, A. Tkachuk, W. B. Yun, *Synchrotron Radiat. News* **2008**, *21*, 17.

[49] M.-Y. Im, H.-S. Han, M.-S. Jung, Y.-S. Yu, S. Lee, S. Yoon, W. Chao, P. Fischer, J.-I. Hong, K.-S. Lee, *Nat. Commun.* **2019**, *10*, 1.

[50] M. Wolfman, Canismarko/xanespy: Chemical imaging of materials using x-ray absorbance spectroscopy, https://github.com/canismarko/xanespy (accessed: June 2020).

[51] S. van der Walt, J. L. Schönberger, J. Nunez-Iglesias, F. Boulogne, J. D. Warner, N. Yager, E. Gouillart, T. Yu, *PeerJ* **2014**, *2*, e453.

[52] N. Otsu, *IEEE Trans. Syst. Man Cybern. Syst.* **1979**, *9*, 62.

[53] L. Li, Y. K. Chen-Wiegart, J. Wang, P. Gao, Q. Ding, Y.-S. Yu, F. Wang, J. Cabana, J. Wang, S. Jin, *Nat. Commun.* **2015**, *6*, 6883.

[54] P. Virtanen, R. Gommers, T. E. Oliphant, M. Haberland, T. Reddy, D. Cournapeau, E. Burovski, P. Peterson, W. Weckesser, J. Bright, S. J. van der Walt, M. Brett, J. Wilson, K. J. Millman, N. Mayorov, A. R. J. Nelson, E. Jones, R. Kern, E. Larson, C. J. Carey, İ. Polat, Y. Feng, E. W. Moore, J. VanderPlas, D. Laxalde, J. Perktold, R. Cimrman, I. Henriksen, E. A. Quintero, C. R. Harris, et al., *Nat. Methods* **2020**, *17*, 261.

[55] J. D. Hunter, *Comput. In Sci. & Eng.* **2007**, *9*, 90.

[56] B. Orvananos, T. R. Ferguson, H.-C. Yu, M. Z. Bazant, K. Thornton, *J. Electrochem. Soc.* **2014**, *161*, A535.

[57] H.-C. Yu, H.-Y. Chen, K. Thornton, *Modell. Simul. Mater. Sci. Eng.* **2012**, *20*, 075008.

[58] A. Nyman, M. Behm, G. Lindbergh, *Electrochim. Acta* **2008**, *53*, 6356.

[59] S. Brown, N. Mellgren, M. Vynnycky, G. Lindbergh, *J. Electrochem. Soc.* **2008**, *155*, A320.

[60] J. Towns, T. Cockerill, M. Dahan, I. Foster, K. Gaither, A. Grimshaw, V. Hazlewood, S. Lathrop, D. Lifka, G. D. Peterson, R. Roskies, J. R. Scott, N. Wilkins-Diehr, *Comput. In Sci. & Eng.* **2014**, *16*, 62.

2300895 (12 of 12)